Monthly Notices
of the
ROYAL ASTRONOMICAL SOCIETY

Mon. Not. R. Astron. Soc. **409,** 2–11 (2010) doi:10.1111/j.1365-2966.2010.17041.x

Cold dust and young starbursts: spectral energy distributions of *Herschel* SPIRE sources from the HerMES survey★

M. Rowan-Robinson,[1]† I. G. Roseboom,[2] M. Vaccari,[3] A. Amblard,[4] V. Arumugam,[5] R. Auld,[6] H. Aussel,[7] T. Babbedge,[1] A. Blain,[8] J. Bock,[8,9] A. Boselli,[10] D. Brisbin,[11] V. Buat,[10] D. Burgarella,[10] N. Castro-Rodriguez,[12,13] A. Cava,[12,13] P. Chanial,[1] D. L. Clements,[1] A. Conley,[14] L. Conversi,[15] A. Cooray,[4,8] C. D. Dowell,[8,9] E. Dwek,[16] S. Dye,[6] S. Eales,[6] D. Elbaz,[7] D. Farrah,[2] M. Fox,[1] A. Franceschini,[3] W. Gear,[6] J. Glenn,[14] E. A. González Solares,[17] M. Griffin,[6] M. Halpern,[18] E. Hatziminaoglou,[19] J. Huang,[20] E. Ibar,[21] K. Isaak,[6] R. J. Ivison,[5,21] G. Lagache,[22] L. Levenson,[8,9] N. Lu,[8,23] S. Madden,[7] B. Maffei,[24] G. Mainetti,[3] L. Marchetti,[3] A. M. J. Mortier,[1] H. T. Nguyen,[8,9] B. O'Halloran,[1] S. J. Oliver,[2] A. Omont,[25] M. J. Page,[26] P. Panuzzo,[7] A. Papageorgiou,[6] H. Patel,[1] C. P. Pearson,[27,28] I. Perez Fournon,[12,13] M. Pohlen,[6] J. I. Rawlings,[26] G. Raymond,[6] D. Rigopoulou,[27,29] D. Rizzo,[1] B. Schulz,[8,23] Douglas Scott,[18] N. Seymour,[26] D. L. Shupe,[8,23] A. J. Smith,[2] J. A. Stevens,[30] M. Symeonidis,[26] M. Trichas,[1] K. E. Tugwell,[26] I. Valtchanov,[15] L. Vigroux,[25] L. Wang,[2] R. Ward,[2] G. Wright,[21] C. K. Xu[8,23] and M. Zemcov[8,9]

[1]*Astrophysics Group, Imperial College London, Blackett Laboratory, Prince Consort Road, London SW7 2AZ*
[2]*Astronomy Centre, Department of Physics & Astronomy, University of Sussex, Brighton BN1 9QH*
[3]*Dipartimento di Astronomia, Università di Padova, vicolo Osservatorio, 3, 35122 Padova, Italy*
[4]*Department of Physics & Astronomy, University of California, Irvine, CA 92697, USA*
[5]*Institute for Astronomy, University of Edinburgh, Royal Observatory, Blackford Hill, Edinburgh EH9 3HJ*
[6]*Cardiff School of Physics and Astronomy, Cardiff University, Queens Buildings, Cardiff CF24 3AA*
[7]*Laboratoire AIM-Paris-Saclay, CEA/DSM/Irfu – CNRS – Université Paris Diderot, CE-Saclay, pt courrier 131, F-91191 Gif-sur-Yvette, France*
[8]*California Institute of Technology, 1200 E. California Blvd, Pasadena, CA 91125, USA*
[9]*Jet Propulsion Laboratory, 4800 Oak Grove Drive, Pasadena, CA 91109, USA*
[10]*Laboratoire d'Astrophysique de Marseille, OAMP, Université Aix-marseille, CNRS, 38 rue Frédéric Joliot-Curie, 13388 Marseille Cedex 13, France*
[11]*Space Science Building, Cornell University, Ithaca, NY 14853-6801, USA*
[12]*Instituto de Astrofísica de Canarias, C/ Via Lactea s/n, E-38200 La Laguna, Tenerife, Spain*
[13]*Departamento de Astrofísica, Universidad de La Laguna (ULL), E-38205 La Laguna, Tenerife, Spain*
[14]*Department of Astrophysical and Planetary Sciences, CASA 389-UCB, University of Colorado, Boulder, CO 80309, USA*
[15]*Herschel Science Centre, European Space Astronomy Centre, Villanueva de la Cañada, 28691 Madrid, Spain*
[16]*Observational Cosmology Lab, Code 665, NASA Goddard Space Flight Center, Greenbelt, MD 20771, USA*
[17]*Institute of Astronomy, University of Cambridge, Madingley Road, Cambridge CB3 0HA*
[18]*Department of Physics & Astronomy, University of British Columbia, 6224 Agricultural Road, Vancouver, BC V6T 1Z1, Canada*
[19]*ESO, Karl-Schwarzschild-Str. 2, 85748 Garching bei München, Germany*
[20]*Harvard–Smithsonian Center for Astrophysics, MS65, 60 Garden Street, Cambridge, MA 02138, USA*
[21]*UK Astronomy Technology Centre, Royal Observatory, Blackford Hill, Edinburgh EH9 3HJ*
[22]*Institut d'Astrophysique Spatiale (IAS), bâtiment 121, Université Paris-Sud 11 and CNRS (UMR 8617), 91405 Orsay, France*
[23]*Infrared Processing and Analysis Center, MS 100-22, California Institute of Technology, JPL, Pasadena, CA 91125, USA*
[24]*School of Physics and Astronomy, The University of Manchester, Alan Turing Building, Oxford Road, Manchester M13 9PL*
[25]*Institut d'Astrophysique de Paris, UMR 7095, CNRS, UPMC Univ. Paris 06, 98bis boulevard Arago, F-75014 Paris, France*
[26]*Mullard Space Science Laboratory, University College London, Holmbury St Mary, Dorking, Surrey RH5 6NT*
[27]*Space Science & Technology Department, Rutherford Appleton Laboratory, Chilton, Didcot, Oxfordshire OX11 0QX*
[28]*Institute for Space Imaging Science, University of Lethbridge, Lethbridge, Alberta T1K 3M4, Canada*
[29]*Astrophysics, Oxford University, Keble Road, Oxford OX1 3RH*
[30]*Centre for Astrophysics Research, University of Hertfordshire, College Lane, Hatfield, Hertfordshire AL10 9AB*

Accepted 2010 May 17. Received 2010 May 17; in original form 2010 April 30

★*Herschel* is an ESA space observatory with science instruments provided by European-led Principal Investigator consortia and with important participation from NASA.

†E-mail: m.rrobinson@imperial.ac.uk; mrr@imperial.ac.uk

ABSTRACT

We present spectral energy distributions (SEDs) for 68 *Herschel* sources detected at 5σ at 250, 350 and 500 μm in the HerMES SWIRE-Lockman field. We explore whether existing models for starbursts, quiescent star-forming galaxies and active galactic nucleus dust tori are able to model the full range of SEDs measured with *Herschel*. We find that while many galaxies (∼56 per cent) are well fitted with the templates used to fit *IRAS*, *Infrared Space Observatory* (*ISO*) and *Spitzer* sources, for about half the galaxies two new templates are required: quiescent ('cirrus') models with colder (10–20 K) dust and a young starburst model with higher optical depth than Arp 220. Predictions of submillimetre fluxes based on model fits to 4.5–24 μm data agree rather poorly with the observed fluxes, but the agreement is better for fits to 4.5–70 μm data. *Herschel* galaxies detected at 500 μm tend to be those with the highest dust masses.

Key words: galaxies: evolution – galaxies: starburst – galaxies: star formation – cosmology: observations – infrared: galaxies.

1 INTRODUCTION

The combination of *Herschel* (Pilbratt et al. 2010) and *Spitzer* data provides us with the first 3–500 μm spectral energy distributions (SEDs) of large samples of galaxies, so that we can determine accurately the masses of cold dust present in a substantial sample of galaxies and search for very young, heavily obscured starbursts. The HerMES wide-area surveys (Oliver et al. 2010a) have been targeted on fields in which we have excellent *Spitzer* data.

Over the past 20 years increasingly sophisticated radiative transfer models for different types of infrared galaxy have been developed, for example for starburst galaxies (Rowan-Robinson & Crawford 1989; Rowan-Robinson & Efstathiou 1993; Silva et al. 1998; Efstathiou, Rowan-Robinson & Siebenmorgen 2000; Takagi, Arimoto & Hanami 2003; Dopita et al. 2005; Siebenmorgen & Krugel 2007), active galactic nucleus (AGN) dust tori (Rowan-Robinson & Crawford 1989; Pier & Krolik 1992; Granato & Danese 1994; Efstathiou & Rowan-Robinson 1995; Rowan-Robinson 1995; Nenkova, Ivezic & Elitzur 2002; Fritz, Franceschini & Hatziminaoglou 2006; Hönig et al. 2006; Nenkova et al. 2008; Schartmann et al. 2008) and quiescent ('cirrus') galaxies (Rowan-Robinson 1992; Siebenmorgen & Krugel 1992; Silva et al. 1998; Dale et al. 2001; Efstathiou & Rowan-Robinson 2003; Dullemond & van Bemmel 2005; Draine & Li 2006; Piovan, Tantalo & Chiosi 2006; Efstathiou & Siebenmorgen 2009). Each of these model types involves at least two significant model parameters so there are a great wealth of possible models, particularly as a galaxy SED may be a mixture of all three types.

Rowan-Robinson & Efstathiou (2009) have shown how these models can be used to understand the interesting diagnostic diagram of Spoon et al. (2007) for starburst and active galaxies, which plots the strength of the 9.7-μm silicate feature against the equivalent width of the 6.2-μm polycyclic aromatic hydrocarbon (PAH) feature for 180 galaxies with *Spitzer* Infrared Spectrograph (IRS) spectra. Increasing depth of the 9.7-μm silicate feature is, broadly, a measure of the youth of the starburst because initially the starburst is deeply embedded in its parent molecular cloud. The detailed starburst model of Efstathiou et al. (2000) shows the evolution of the starburst SED through the whole history of the starburst, from the deeply embedded initial phase through to the Sedov expansion phase of the resulting supernovae. However, Rowan-Robinson and Efstathiou did find that there was some aliasing between young starbursts and heavily obscured AGN: the submillimetre data of *Herschel* can help to break this ambiguity since young starbursts are expected to be much more prominent in the far-infrared and submillimetre than AGN dust tori.

Often, however, we have only limited broad-band data available and in this situation it is more illuminating to use a small number of infrared templates to match the observed infrared colours (e.g. Rowan-Robinson & Crawford 1989; Rowan-Robinson 1992, 2001; Rowan-Robinson & Efstathiou 1993; Rowan-Robinson et al. 2004, 2005, 2008). A set of just four templates (a quiescent 'cirrus' component, M82- and Arp 220-like starbursts and an AGN dust torus model) have proved remarkably successful in matching observed *Infrared Space Observatory* (*ISO*) and *Spitzer* SEDs, including cases where *Spitzer* IRS data are available (Rowan-Robinson et al. 2006; Farrah et al. 2008; Hernan-Caballero et al. 2009). In this paper we explore whether this simple four-template approach works for galaxies detected by the Spectral and Photometric Imaging Receiver (SPIRE) array (Griffin et al. 2010) on *Herschel*, and what additional infrared components may be present.

A cosmological model with $\Lambda = 0.7$, $h_0 = 0.72$ has been used throughout.

2 SELECTION OF SAMPLE WITH GOOD-QUALITY FLUXES AT 24, 250, 350 AND 500 μm

In this analysis we have focused on early HerMES[1] (Oliver et al. 2010a) Science Demonstration data in the SWIRE-Lockman area, where we have optical and 3.6–160 μm photometry, photometric redshifts and infrared template fits from the SWIRE Photometric Redshift Catalogue (Rowan-Robinson et al. 2008). Obviously we are particularly interested in whether any new galaxy populations can be seen in the *Herschel* data.

Photometry in the SPIRE bands was carried out via a linear inversion of the SPIRE maps, using the positions of known 24-μm sources and the SPIRE point-source response function (PSF) as an input. The PSF was assumed to be a Gaussian with full width to half-power of 18.2, 25.2 and 36.3 arcsec at 250, 350 and 500 μm,

[1] http://hermes.sussex.ac.uk

respectively. The 24-μm input catalogue was optimized to alleviate concerns about overfitting. The method and description of the catalogue are presented in Roseboom et al. (2010). In the 5-deg^2 SWIRE-Lockman area, 5225 sources were detected at 5σ in at least one band and 2367 of these are associated with sources in the SWIRE Photometric Redshift Catalogue. We have focused on the 70 sources detected at 5σ in all three SPIRE bands, which also satisfy some further restrictions. Specifically, we use the recommended selections described in Roseboom et al. (2010) which ensure robust solutions from the inversion process, i.e. low χ^2 and minimal correlations with neighbouring sources. This is essentially a 500-μm selected sample, with a flux limit of ∼27 mJy. The combination of PSF fitting, the choice of 24-μm targets only and the elimination of confused sources allows us to reach fainter fluxes than would be possible in an unbiased survey. Our requirement of association with a SWIRE 24-μm source discriminates against sources with $S(500)/S(24) > 200$, and our requirement of an entry in the SWIRE Photometric Redshift Catalogue discriminates against sources with $z > 1.5$. Selection at 500 μm favours galaxies with cooler dust than say selection at 70 or even 250 μm. From HerMES counts at 500 μm (Oliver et al. 2010b) we deduce that there should be 124 ± 16 500 μm sources brighter than this flux in the 5-deg^2 area of this study. Thus our sample represents 46–66 per cent of the total 500-μm population. The remaining sources are presumably fainter than the limit of the SWIRE optical photometry ($r \sim 25$) or the SWIRE 24-μm limit [$S(24) \sim 100$ μJy]. Since confusion is an issue, particularly at 500 μm, we have carefully examined all 24-μm sources within 40 arcsec of SPIRE sources to assess whether these neighbours could have contributed significantly to the 500-μm flux. We eliminated two of the 70 sources as having neighbours likely to have contributed >30 per cent of the 500-μm flux.

3 SPECTRAL ENERGY DISTRIBUTIONS OF *HERSCHEL* GALAXIES

We have modelled the SEDs of the remaining 68 three-band sources, following the methodology of Rowan-Robinson et al. (2008), and the results are presented in Figs 1–6, in redshift order. Optical and near-infrared data are fitted with one of the six galaxy templates and two QSO templates, with the extinction A_V as a free parameter. Infrared and submillimetre data are fitted initially with a combination of four infrared templates (cirrus, M82 and A220 starbursts or AGN dust torus). Properties of the SED templates used are given in Table 1, and parameters of the fits are given in Table 2. Some unpublished spectroscopic redshifts were supplied by Huang et al. (in preparation). Photometric redshifts have been indicated in Figs 1–6 and Table 2 with brackets. The accuracy of these redshifts is ∼5 per cent in $(1+z)$ for most of the galaxies, where four or more photometric bands are available (Rowan-Robinson et al. 2008). The full χ^2 distribution for the photometric redshifts is given in the SWIRE Photometric Redshift Catalogue. The optical galaxy templates are those of Rowan-Robinson et al. (2008) and are shown at full resolution in the SED plots. The optical types given in Table 2 are

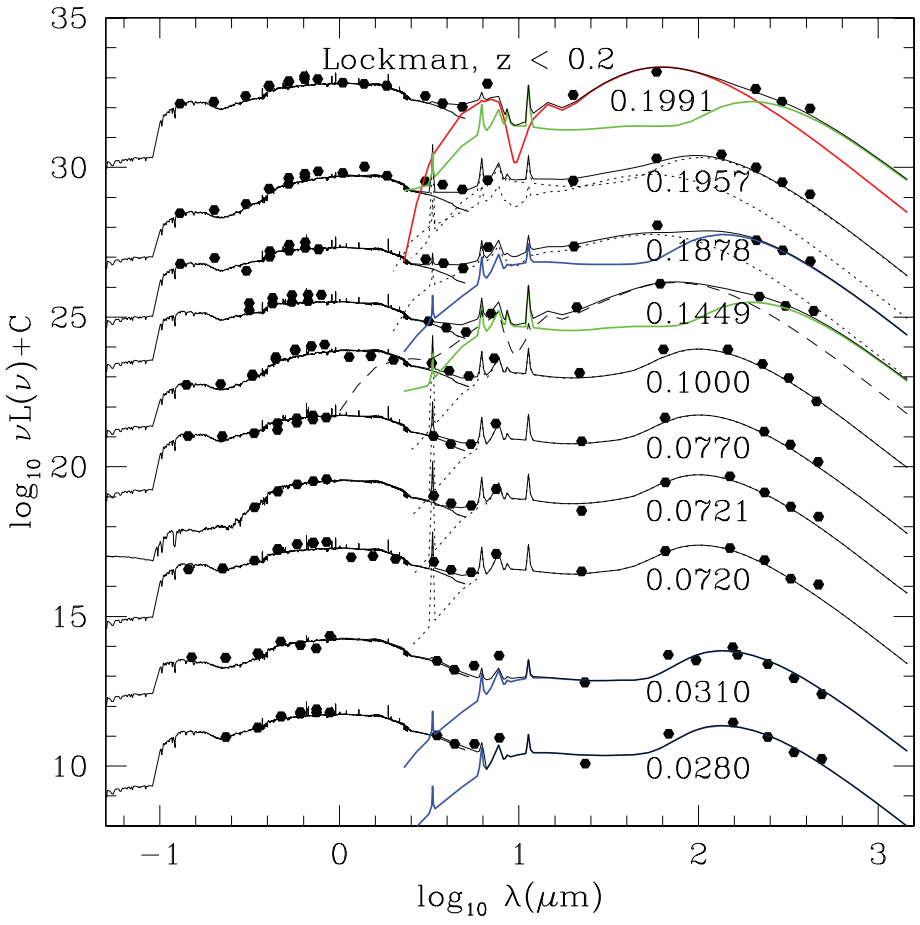

Figure 1. SEDs for SWIRE-Lockman three-band galaxies with $z < 0.2$, labelled with their redshift (all are spectroscopic). Blue and green curves are quiescent ('cirrus') model with colder dust ($\psi = 1, 0.1$). The red curve is a young starburst model.

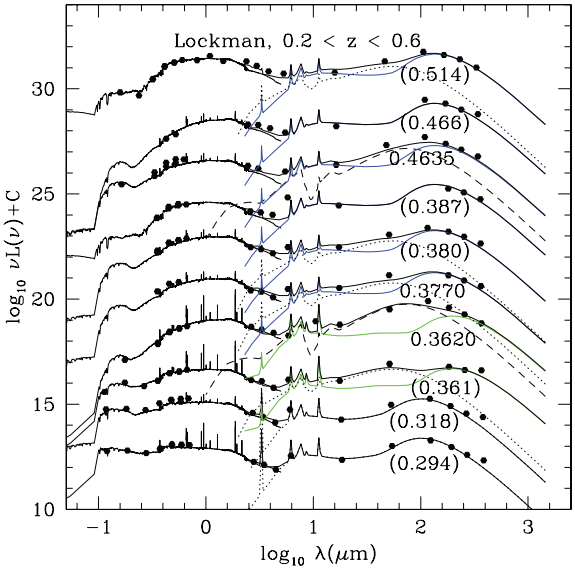

Figure 2. SEDs for SWIRE-Lockman three-band galaxies with $0.2 < z < 0.5$. Photometric redshifts are indicated with brackets.

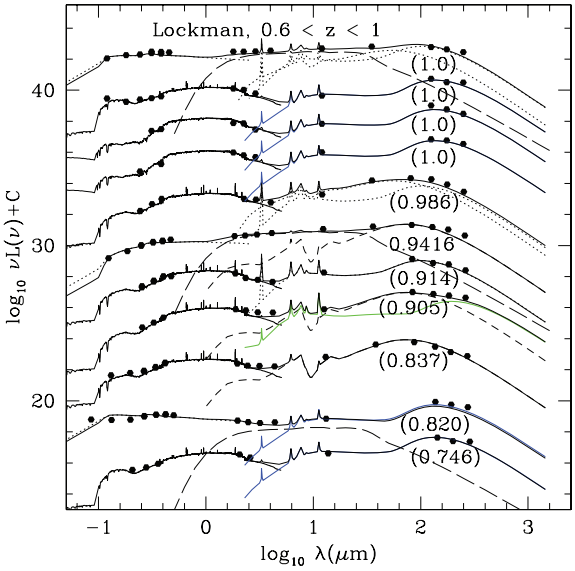

Figure 3. SEDs for SWIRE-Lockman three-band galaxies with $0.5 < z < 1$.

optical template types only and contain no morphological information. None of the 68 objects is radio-loud AGN and none shows evidence for non-thermal emission at 3.6–500 μm.

While the four standard infrared templates work well for many sources, the 350- and 500-μm fluxes often require the presence of colder dust than is incorporated into our four basic templates. The two new templates used here are taken from the range of optically thin interstellar medium ('cirrus') templates developed by Rowan-Robinson (1992) and Efstathiou & Rowan-Robinson (2003). The key parameter determining the temperature of the dust grains is the intensity of the radiation field, which we can characterize by the ratio of intensity of radiation field to the local interstellar radiation field, ψ. The standard cirrus template corresponds to $\psi = 5$, and this is the value used by Rowan-Robinson (1992) to fit the central regions of our Galaxy. $\psi = 1$ corresponds to the interstellar radiation field in the vicinity of the Sun. We also find that some galaxies

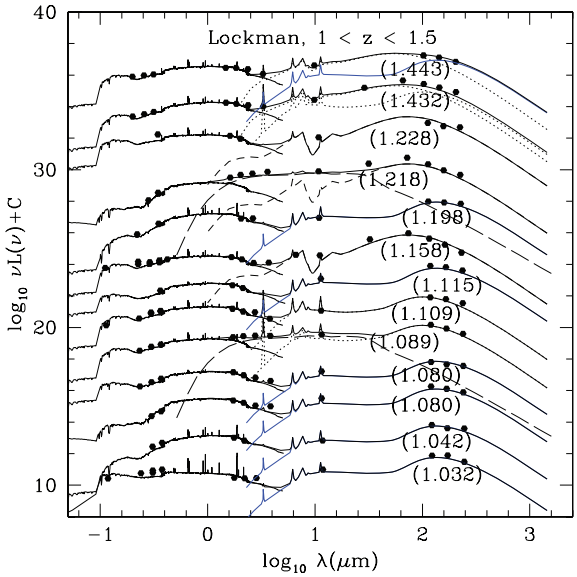

Figure 4. SEDs for SWIRE-Lockman three-band galaxies with $1 < z < 1.5$.

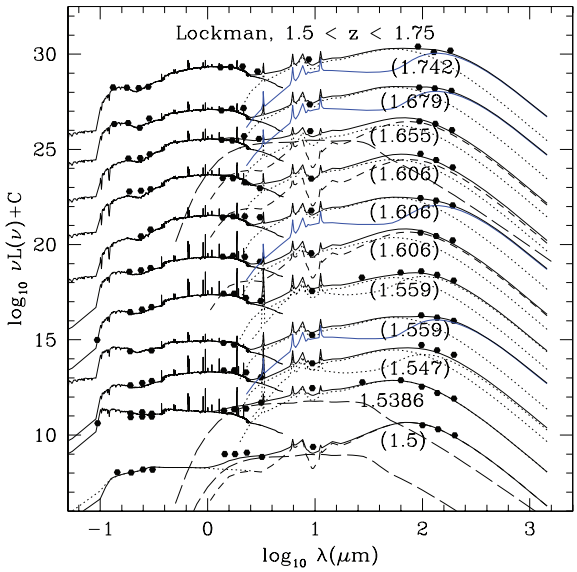

Figure 5. SEDs for SWIRE-Lockman three-band galaxies with $1.5 < z < 1.75$.

need a much lower intensity radiation field than this, with $\psi = 0.1$. The corresponding grain temperatures in the dust model of Rowan-Robinson (1992) are given in Table 1. For the two new templates, the range of dust grain temperatures are 14.5–19.7 and 9.8–13.4 K, respectively. Full details of the templates used are given at http://astro.ic.ac.uk/∼mrr/spire/templates.

The need for cooler dust templates can also be seen clearly in a plot of $S(500)/S(24)$ versus redshift (Fig. 7), in which the predictions of different templates are shown. At $z < 1$, a significant fraction of galaxies requires colder dust than the standard cirrus model. Hints of this population were seen at $z < 0.4$ in the plot of *ISO* 175/90 μm flux ratio versus redshift (fig. 23 of Rowan-Robinson et al. 2004). Symeonidis et al. (2009) plotted a very similar figure, 160/70 μm flux ratio versus redshift, for *Spitzer* data. They interpreted this as implying strong evolution in the cold dust component.

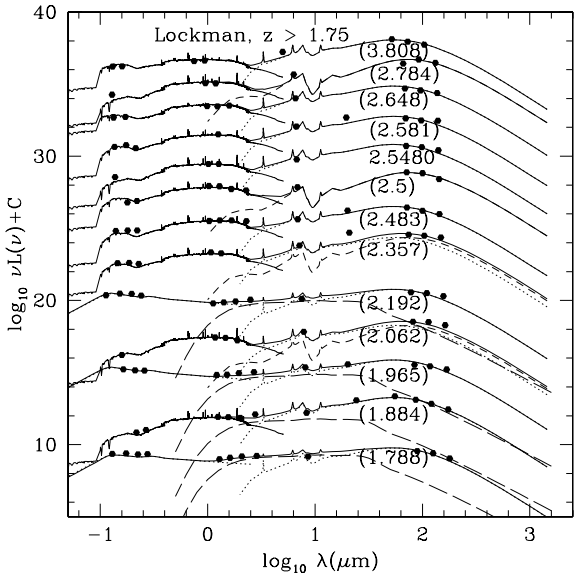

Figure 6. SEDs for SWIRE-Lockman three-band galaxies with $z > 1.75$.

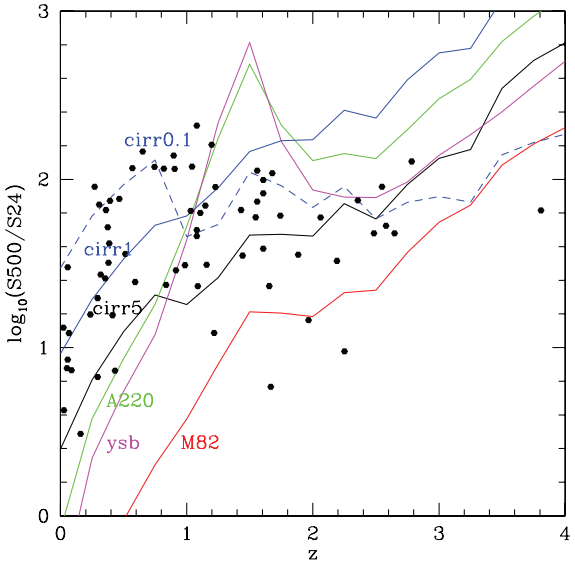

Figure 7. The (500/24) μm flux ratio versus z. Black filled circles: SPIRE-Lockman sources detected at better than 5σ at 250, 350 and 500 μm. Continuous loci: predictions of infrared templates – black: cirrus ($\psi = 5$); red: M82 starburst; green: A220 starburst; blue: cooler cirrus ($\psi = 1$); blue broken line: colder cirrus ($\psi = 0.1$) and magenta: young starburst ($A_V = 150$, $t = 0$).

Table 1. Colour temperature, dust grain temperatures and peak wavelengths of the templates used here.

Template	'T_d' ($\nu^2 B_\nu(T_d)$) (K)	Actual dust temperature (K)	Peak λ (μm)	60-μm bol. correction
Cirrus $\psi = 0.1$	12	9.8–13.4	202	10.9
Cirrus $\psi = 1$	17.5	14.5–19.7	136	8.38
Cirrus $\psi = 5$	23.5	19.1–24.1	102	3.30
Arp 220 sb	33	3–1000	73	1.50
Young sb ($t = 0$)	38	3–1000	63	1.28
M82 sb	45	3–1000	53	1.75

18 of the 68 sources modelled in Figs 1–6 are '350-μm peakers' [$S(250) < S(350)$, $S(500) < S(350)$]. All are at redshift > 0.9 and 10 have $z > 1.5$. Six, which are given as lower redshift (<0.5) in the SWIRE Photometric Redshift Catalogue, clearly require higher redshift to fit their SEDs. In each of these cases the photometric redshift was based on only two photometric bands, so of very low reliability. The adopted redshifts for these six galaxies are indicated in brackets in Table 1 with only two significant figures. The remaining photometric redshifts appeared plausible from the SED fits. Five of the 68 sources are '500-μm peakers' [$S(250) < S(350) < S(500)$]: all of these are at $z > 0.9$, and three are at $z > 1.5$. So 350- and 500-μm peakers are a reasonably good indication of high redshift. However, the range of infrared template required makes any determination of redshift from *Herschel* data alone problematic. The six templates, $\psi = 0.1$ cirrus, $\psi = 1$ cirrus, $\psi = 5$ cirrus, Arp 220 starburst, $t = 0$ starburst and M82 starburst, have their νS_ν peaks at 202, 136, 102, 73, 63 and 53 μm, respectively, which could give rise to a range of a factor of 3.8 in the determined $(1 + z)$.

For a few sources plotted in Figs 1–6, the 500-μm point lies higher than the template fits. This is probably due to residual effects of confusion at 500 μm. Four sources in Figs 6 and 8 have observed fluxes highly discrepant with the models, three of which are *Spitzer* 70-μm fluxes. These require further investigation.

Since only one of the three-band samples has $z > 3$, we have selected all SWIRE-Lockman galaxies with $z > 3$ detected at 5σ at 250 and 350 μm. There are 15 of them (including the three-band source) and Fig. 8 shows SEDs for 11 of them. 500-μm fluxes are included if they are better than 3σ. Nine are hyperluminous ($L_{ir} > 10^{13}\,L_\odot$) M82-like starbursts, four of these with AGN dust tori and just two are Arp 220-like starbursts. None of these $z > 3$ galaxies shows evidence of the cold dust components seen at lower redshift, but this is an effect of the redshift since the rest-frame wavelength corresponding to the SPIRE bands is at ≤100 μm. We show a young starburst fit for one of the objects (see below). It would be an acceptable alternative to the M82 starburst fit for this object and perhaps for a couple of others. Additional photometry will clarify this ambiguity. The other templates are reasonably distinct in their peak wavelength (see Table 1) so less susceptible to aliasing. Where the 500-μm fluxes are less than 3σ we have checked that the model fits are consistent with the 3σ limits.

To search for young starbursts, previously indicated by IRS spectra with very deep silicate features (Rowan-Robinson & Efstathiou 2009), we show a plot of $S(70)/S(24)$ versus redshift for the 360 sources detected at 5σ at 70, 250 and 350 μm, compared with the predictions of existing templates (Fig. 9). There is a clear population of sources showing deeper 10-μm absorption than the Arp 220 template, and we have modelled the SEDs of a selection of these in Fig. 10. All nine sources have very similar SEDs, with warm 100–500 μm colours but relatively weak 24-μm fluxes, and are well fitted with a very young starburst model. Sources in the redshift range of 1.35–1.45 for which 24 μm would fall in the deep silicate absorption would be discriminated against by their faintness at 24 μm. To confirm the reality of this component we need to obtain SPIRE photometry of sources identified as having very deep silicate features from *Spitzer* IRS observations. To identify these young starbursts we need both *Spitzer* and *Herschel* data. They can be masked by additional cirrus emission in the galaxy, as in the case of 161.34665+57.51625 in Fig. 1.

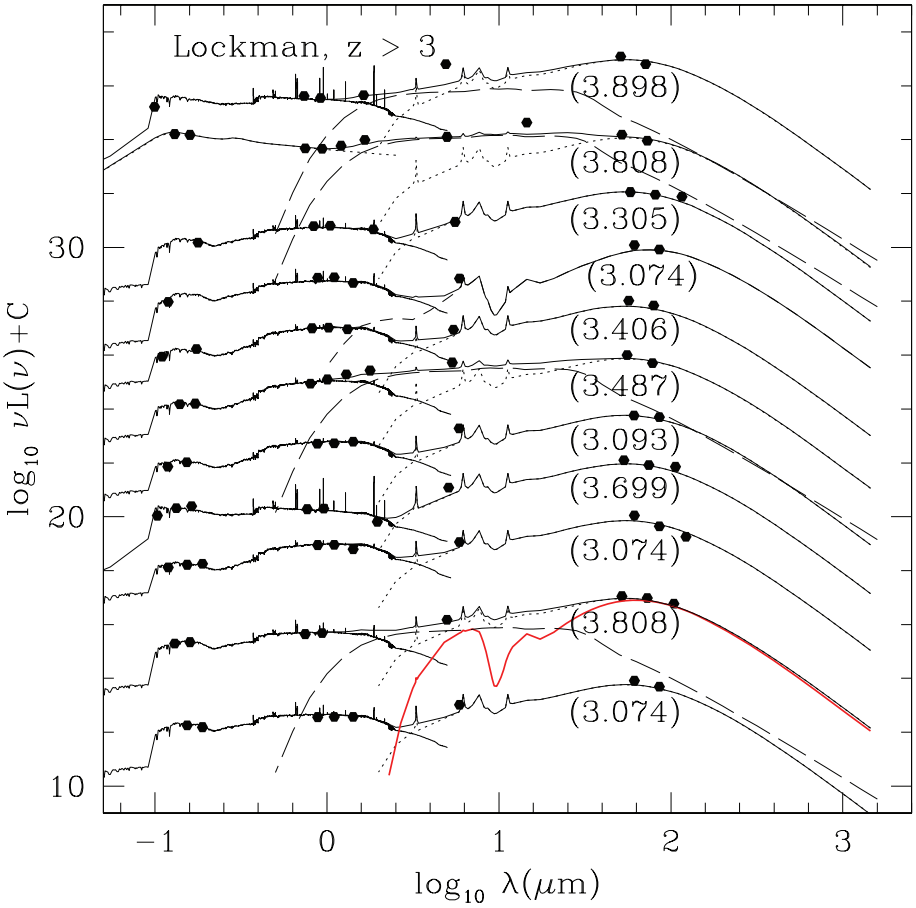

Figure 8. SEDs for SWIRE-Lockman 250+350 μm galaxies with $z > 3$.

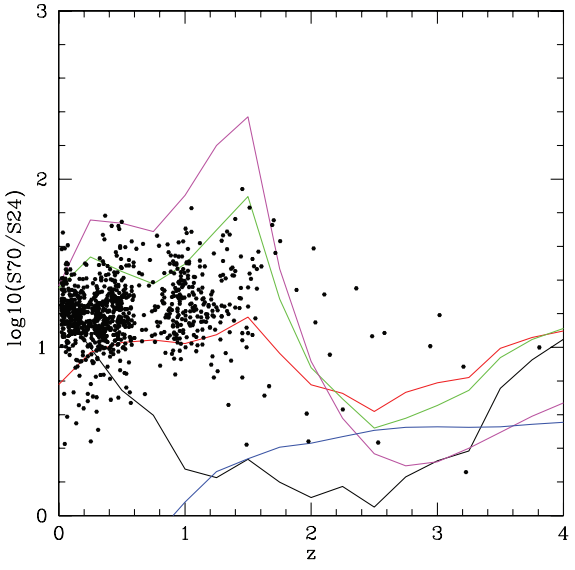

Figure 9. [70/24] versus z. Filled circles: SPIRE-Lockman sources detected at better than 5σ at 70, 250 and 350 μm. Colour coding for model loci as in Fig. 1.

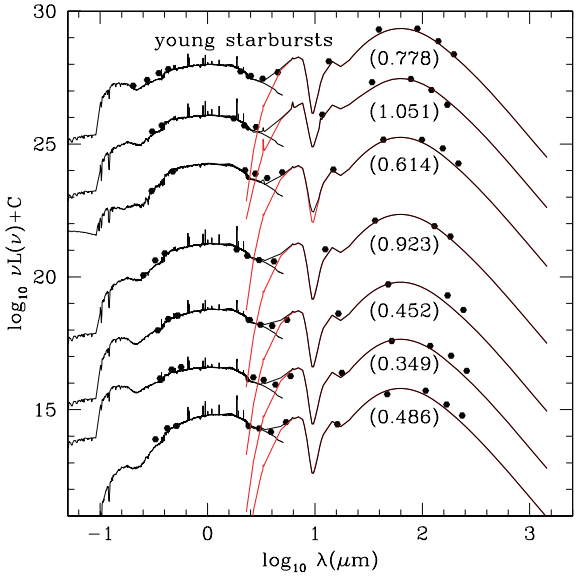

Figure 10. SEDs for SPIRE-Lockman galaxies with [70/24] > 1.5. Red curves are models for very young starbursts.

Fig. 11 shows infrared luminosity versus redshift for all the infrared components listed in Table 2. If a galaxy is fitted with several components, each is shown separately here. Cirrus components, including the new colder templates, are seen at redshifts out to 1.7 and at luminosities up to $\sim 10^{12}\,L_{\odot}$. Higher redshift galaxies may also have cool dust components, but we would need photometry at $\lambda > 500\,\mu$m to characterize them. Higher luminosity sources are generally M82 or A220 starbursts, but the latter do not dominate

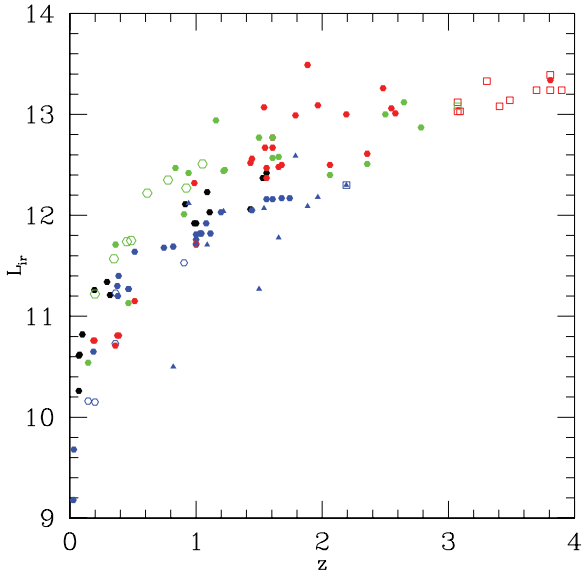

Figure 11. Infrared luminosities of different components as function of redshift. Filled black hexagons: cirrus ($\psi = 5$), filled blue hexagons: cirrus ($\psi = 1$), open blue hexagons: cirrus ($\psi = 0.1$), filled red hexagons: M82 starbursts, filled green hexagons: Arp 220 starbursts, open green hexagons: young starbursts, open red squares: additional $z > 3$ M82 starbursts, open green square: additional $z > 3$ Arp 220 starburst and filled blue triangles: AGN dust tori.

amongst hyperluminous ($L_{\rm ir} > 10^{13}\,{\rm L}_\odot$) galaxies. The young starbursts are seen at $z = 0.2$–1.1 and are amongst the highest luminosity objects in their redshift range, but this is partially a selection effect because of the requirement of a 70-μm detection. Young starbursts may also be present in higher redshift objects (see e.g. Fig. 8), where additional photometry would be needed to eliminate aliasing with an M82 starburst.

We can compare the predicted submillimetre fluxes from the SWIRE Photometric Redshift Catalogue template fits with the observed *Herschel* fluxes. Fig. 12 shows this comparison at 250 μm for fits based on 4.5–24 μm data only and for fits based on 4.5–70 μm data, in both cases restricting to sources detected with at least 5σ at 250 μm and excluding sources with infrared SEDs dominated by an AGN dust torus. The 4.5–70 μm fits show some correlation, with a tendency to underestimate the fluxes because of the failure to account for colder dust. The average value of $\log_{10}(S(250)_{\rm obs}/S(250)_{\rm pred})$ is 0.075, corresponding to a mean underestimate by a factor of 1.2, with an rms scatter of 0.38 dex. Predictions based on 4.5–24 μm only data show a larger scatter compared with the observed fluxes. The average value of $\log_{10}(S(250)_{\rm obs}/S(250)_{\rm pred})$ is 0.37, corresponding to a larger mean underestimate by a factor of 2.35, with an rms scatter of 0.51 dex. This reflects the fact that there was no possibility of predicting the presence of 10–20 K dust from observations at 4.5–24 μm. Note that these mean ratios are biased by the observed 250-μm flux limit. The correlation is worse at 500 μm. Elbaz et al. (2010) address a slightly different issue: how well the bolometric luminosity, derived at 100–500 μm, is correlated with the 24-μm luminosity. They found a good correlation, but also that 250- and 350-μm monochromatic luminosities deviated (on the high side) from their template predictions (their fig. 2). Our explanation for that deviation is the presence of the new cold dust components.

4 DISCUSSION

By combining *Herschel* 250–500 μm data with *Spitzer* 3.6–160 μm data we have demonstrated the presence of two new infrared components in galaxy SEDs: a colder quiescent ('cirrus') component, and a very young starburst component. Local *IRAS* galaxies with colder cirrus than our standard $\psi = 5$ cirrus template were discussed previously by Rowan-Robinson (1992). Cooler dust was also inferred from *ISO* 200-μm mapping of eight nearby galaxies by Alton et al. (1998). They inferred a grain temperature of 18–21 K for this extended, colder component. *ISO* 175/90 μm versus z (Rowan-Robinson et al. 2004) and *Spitzer* 160/70 μm versus z (Symeonidis et al. 2009) diagrams can be interpreted as pointing to cooler dust in galaxies at $z < 0.4$. Here we find cooler dust to be present to a much higher range of luminosities ($10^{12}\,{\rm L}_\odot$) and redshift (1.7). Cold dust could be present in high-redshift ($z > 3$) galaxies but would be observable only at wavelengths >500 μm. The possibility that a significant fraction of galaxies detected at 850 μm could be fitted by a cirrus template was highlighted by Efstathiou & Rowan-Robinson (2003). The new colder cirrus templates we are using here have dust grains at temperatures 10–20 K for different grain types (see Table 1). Colder dust implies lower surface brightness illumination, and therefore more extended emission than the standard templates.

We have estimated the dust and stellar masses for these 68 galaxies, using the prescriptions of Rowan-Robinson et al. (2008). The star formation histories used to generate the optical templates yield the ratio of bolometric (or monochromatic) luminosity to stellar mass at $z = 0$. Rowan-Robinson et al. (2008) give a simple prescription to correct this ratio at earlier times for the effects of passive stellar evolution. The radiative transfer models for the infrared templates predict the ratio of bolometric infrared luminosity to dust mass. Fig. 13 shows dust mass versus stellar mass for *Herschel* galaxies compared with the distribution for *Spitzer*–SWIRE galaxies. All the galaxies with $M_{\rm dust} < 3 \times 10^8\,{\rm M}_\odot$ have $z < 0.3$. Apart from these low-redshift, low-luminosity, lower dust mass galaxies, *Herschel* 500-μm galaxies tend to be those galaxies with the very highest dust masses amongst the galaxies detected by *Spitzer*. Assuming standard gas-to-dust ratios, they must have exceptionally high ratios of gas mass to stellar mass.

At low redshifts ($z < 0.2$) and luminosities ($L_{\rm ir} < 10^{11}\,{\rm L}_\odot$), we find $L_{\rm ir} < L_{\rm opt}$, consistent with emission from an optically thin interstellar medium. However, at higher redshifts and luminosities we find cirrus components with $L_{\rm ir}/L_{\rm opt}$ ranging up to 5, suggesting an optical depth in cold dust $\tau_{\rm uv}$ of at least 1–2. For 41 of our 68 galaxies we infer dust extinctions in the range $A_V = 0.2$–2, corresponding to an ultraviolet (1000 Å) optical depth $\tau_{\rm uv} \sim 1$–10 for normal Galactic dust. This is consistent with the values deduced by Buat et al. (2010) from comparison of SPIRE and *GALEX* data. However, we also have nine examples of galaxies at $z = 0.4$–1.1 with cirrus components with high $L_{\rm ir}/L_{\rm opt}$, but in which the optical starlight appears unreddened, including five fitted with elliptical galaxy templates in the optical. We have to presume illumination of the cold dust is not by the stars contributing to the optical continuum, but by an obscured stellar population. For normal Galactic dust, the spatial scale of the dust must be tens of kiloparsecs. A *Spitzer* population of elliptical galaxies with $L_{\rm ir} > L_{\rm opt}$ was discussed by Rowan-Robinson et al. (2008, see fig. 20). The optical and infrared components seem to be unconnected with each other, perhaps reflecting a galaxy merger. Another possibility would be that the optical galaxy is lensing a background submillimetre galaxy.

Table 2. Parameters for SED models, complete sample of 68 three-band sources (luminosities and dust masses are in $\log_{10}$ solar units).

RA	Dec.	z	$L_{\rm cirr},\ \psi = 5$	$L_{\rm cirr},\ \psi = 1$	$L_{\rm sb,M82}$	$L_{\rm sb,A220}$	$L_{\rm tor}$	$L_{\rm opt}$	Template	A_V	$M_{\rm dust}$
162.94820	58.26883	0.0280		9.18				9.79	Scd	0.25	6.99
161.11473	58.90322	0.0310		9.68				10.19	Sab	0.0	7.49
159.98526	57.40519	0.0720	10.26					10.36	Scd	0.2	7.37
160.10109	58.15504	0.0721	10.61					10.46	E	0.0	7.72
164.36295	57.94135	0.0770	10.62					10.82	Scd	0.3	7.73
160.46895	58.97295	0.1000	10.82					10.92	Sab	0.4	7.93
162.21977	59.63440	0.1449		10.16[a]		10.54		10.09	Scd	0.0	8.98
161.11208	57.70857	0.1878		10.65	10.76			10.46	Scd	0.2	8.47
158.99170	58.97944	0.1957	11.26		10.76			10.81	Sab	0.5	8.38
161.34665	57.51625	0.1991		10.15[a]		11.22[b]		10.96	Scd	0.3	8.98
162.41336	57.68822	(0.294)	11.34					11.23	sb	0.0	8.32
159.88918	59.07882	(0.318)	11.21					11.23	Scd	0.0	9.54
160.00403	57.31637	(0.361)		10.73[a]	10.71			11.11	sb	0.8	9.54
162.80595	57.24055	0.3620		11.23[a]		11.71		11.61	sb	1.9	10.05
160.35732	59.34703	0.3770		11.30	10.81			11.26	Scd	1.0	9.11
162.35535	57.92122	(0.380)		11.20	10.81			11.26	Scd	1.0	9.01
161.11140	59.45845	(0.387)		11.40				10.62	E	0.0	9.21
162.11961	58.27710	0.4635		11.27		11.13		10.87	Scd	0.75	9.10
163.17931	58.67978	(0.466)		11.27				10.93	Scd	1.8	9.08
161.72240	59.65389	(0.514)		11.64	11.15			11.50	E	0.0	9.45
161.32074	58.78179	(0.746)		11.68				10.99	Scd	0.8	9.49
162.54356	57.91158	(0.820)		11.69			10.50	11.60	QSO	0.2	9.50
160.39917	58.65377	(0.837)				12.47		11.32	Sbc	0.0	9.11
160.97595	59.36114	(0.905)		11.53[a]		12.01		11.21	Sbc	0.6	10.35
161.62852	57.54497	(0.914)	12.11					11.56	Sbc	0.2	9.22
160.51041	58.67371	0.9416				12.42	12.12	12.12	QSO	0.8	9.06
161.28079	57.89500	(0.986)	11.92		12.32			11.55	Sbc	0.2	9.11
160.76065	58.44792	(1.0)		11.81				11.22	E	0.0	9.62
162.94107	58.85802	(1.0)		11.81				11.32	E	0.0	9.62
161.44548	59.58356	(1.0)		11.71				11.52	Scd	0.5	9.52
159.70134	58.61901	(1.0)	11.92		11.72		11.72	11.92	QSO	0.3	9.05
163.31041	58.25547	(1.032)		11.81				11.22	sb	0.15	9.62
158.92084	57.47687	(1.042)		11.82				11.38	Sbc	0.4	9.63
159.27916	57.51514	(1.080)		12.17				11.62	E	0.0	9.98
162.93555	58.62388	(1.080)		11.92				11.38	Sab	0.0	9.73
159.02222	59.17973	(1.089)	12.23				11.71	11.59	Scd	0.3	9.34
159.12962	58.90953	(1.109)	12.03					11.63	Scd	0.3	9.14
159.05000	58.45025	(1.115)		11.82				10.98	Sbc	0.0	9.63
162.70114	57.71767	(1.158)				12.94		11.84	Scd	0.2	9.58
159.70450	58.38959	(1.198)		12.03				11.46	Sbc	0.4	9.84
162.19649	57.39379	(1.218)				12.44	12.04	11.33	E	0.0	9.08
161.19606	57.60232	(1.228)				12.45		11.50	Scd	0.0	9.07
159.49042	57.76735	(1.432)	12.06		12.52			11.65	Scd	0.45	9.25
161.24333	57.55045	(1.443)		12.05	12.56			11.89	Scd	0.25	9.88
162.01488	58.90593	(1.5)				12.77	11.27	11.17	QSO	0.6	9.39
158.80722	57.57902	1.5386			13.07		12.07	11.72	sb	0.2	9.11
163.39421	57.71170	(1.547)	12.37		12.67			11.93	sb	0.8	9.54
160.05550	58.52735	(1.559)		12.16	12.37			11.25	Scd	0.2	9.98
163.81096	57.99709	(1.559)	12.47		12.47			12.02	sb	1.0	9.62
161.86531	57.94479	(1.606)			12.57	12.77		11.97	sb	0.9	9.47
164.09378	58.25208	(1.606)		12.16	12.67			11.78	Sbc	0.2	9.99
159.06248	57.91819	(1.606)			12.67	12.57		11.90	Sbc	0.1	9.33
163.18320	58.37976	(1.655)			12.48	12.58	11.78	11.78	Sbc	0.1	9.30
160.54668	59.17580	(1.679)		12.17	12.48			11.48	Scd	0.4	9.99
162.10071	59.34946	(1.742)		12.17	12.48			11.78	Scd	0.8	9.99
162.33145	58.98063	1.7880			12.99		12.59	12.69	QSO	0.1	9.03
162.91730	58.80596	(1.884)			13.49		12.09	12.13	Sbc	0.1	9.53
161.54591	58.16109	(1.965)			13.09		12.18	12.56	QSO	0.0	9.13
159.22012	58.31201	(2.062)			12.50	12.40		11.70	Sbc	0.1	9.16
162.36497	59.06819	(2.192)			13.00		12.30	12.70	QSO	0.0	9.04
164.85812	58.30039	(2.357)			12.61	12.51		11.65	Scd	0.4	9.27
159.61342	57.87177	(2.483)			13.26			12.45	Scd	0.55	9.30
163.17749	58.66597	(2.5)				13.00		12.25	Scd	0.5	9.64

Table 2 – *continued*

RA	Dec.	z	$L_{\mathrm{cirr},\psi=5}$	$L_{\mathrm{cirr},\psi=1}$	$L_{\mathrm{sb,M82}}$	$L_{\mathrm{sb,A220}}$	L_{tor}	L_{opt}	Template	A_V	M_{dust}
162.84056	57.70921	2.5480			13.06			11.71	Sbc	0.0	9.10
161.54903	59.04079	(2.581)			13.01			11.90	Scd	0.5	9.05
161.45622	57.56762	(2.648)				13.12		11.85	Sab	0.0	9.76
161.85199	59.06105	(2.784)				12.87		11.41	Sbc	0.0	9.51
163.07271	58.98540	(3.808)			13.34			12.08	Scd	0.0	9.38
Young sb											
161.65623	57.73351	(0.486)				11.75[b]		11.04	Sbc	1.0	8.27
162.53716	57.82069	(0.349)				11.57[b]		10.81	Scd	0.4	8.09
159.67081	57.94089	(0.452)				11.74[b]		11.07	Scd	0.8	8.26
161.55408	58.09828	(0.923)				12.37[b]		11.45	Sbc	0.3	8.89
159.75601	58.53660	(0.614)				12.22[b]		11.32	E	0.0	8.74
163.56523	58.70536	(1.051)				12.51[c]		11.26	Sbc	0.0	9.03
160.28583	58.77047	(0.778)				12.35[b]		11.29	Scd	0.4	8.87
$z > 3$											
164.67636	57.55608	(3.074)			13.03			12.03	Scd	0.0	9.07
159.28676	57.65699	(3.808)			13.24		12.24	12.09	Scd	0.0	9.28
						13.05[b]	12.24	12.09	Scd	0.0	9.57
159.18820	58.03481	(3.074)			13.12			12.28	Sab	0.0	9.16
164.53999	58.03517	(3.699)			13.24			11.79	sb	0.0	9.28
161.60800	58.23610	(3.093)			13.03			12.08	Sab	0.1	9.07
163.42009	58.61931	(3.487)			13.14		12.88	12.36	Sab	0.1	9.18
162.51204	58.11813	(3.406)			13.08			12.33	Sab	0.0	9.12
163.03342	58.16816	(3.074)				13.08		12.15	Scd	0.15	9.72
164.52054	58.30782	(3.305)			13.33			12.13	Scd	0.1	9.37
159.67590	59.01916	(3.808)			13.34		13.52	13.52	QSO	0.0	9.38
161.78809	58.72614	(3.898)			13.24		12.24	12.04	sb	0.0	9.28

[a] $\psi = 0.1$.
[b] Young sb, $t = 0$.
[c] ysb, $t = 6$ Gyr.

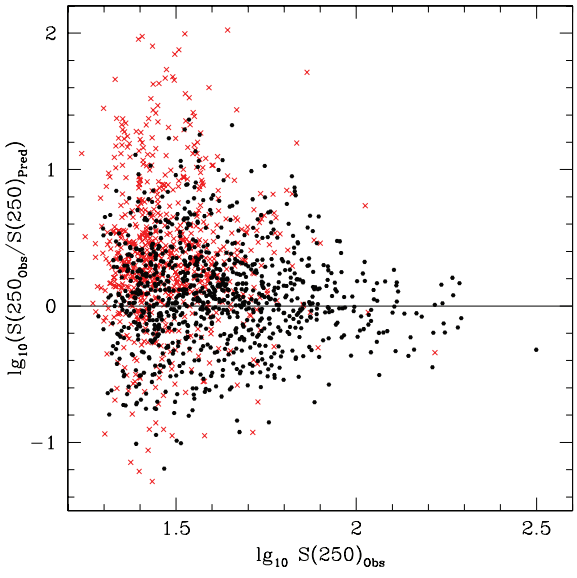

Figure 12. Ratio of observed flux at 250 μm to predicted flux, based on 4.5–24 μm data, versus observed 250-μm flux (red crosses). Filled black circles are predictions based on 4.5–70 μm data.

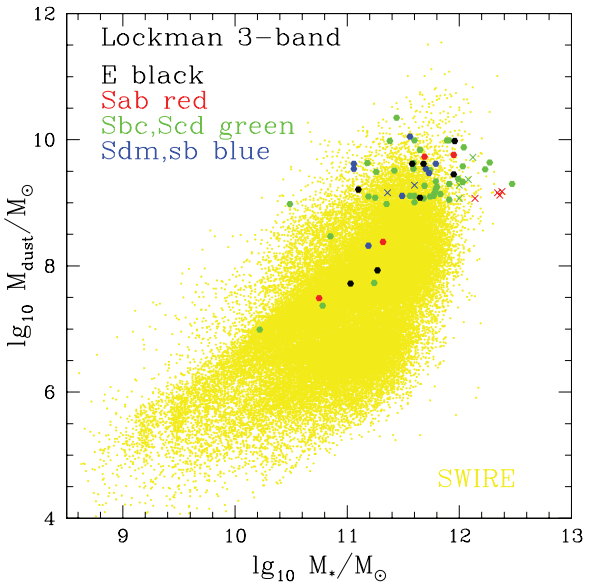

Figure 13. Dust mass versus stellar mass for *Herschel* SPIRE galaxies (large filled circles), compared with distribution for SWIRE Photometric Redshift Catalogue (small yellow circles).

Very young starbursts were invoked by Rowan-Robinson & Efstathiou (2009) to understand the galaxies with deepest silicate absorptions in their IRS spectra. The combination of it with *Herschel* and *Spitzer* data allows us to identify very young starbursts from their SED, even where we do not have detailed mid-infrared spectroscopy, and holds out the prospect of determining an age sequence among starbursts. So far we have identified these only to $z \sim 1$, but this is a selection effect due to the need to have a SWIRE 70-μm detection. Larger samples at $z > 2$, and photometry over the full range of wavelength from 70 to 1100 μm, will be needed to characterize the evolution of these different populations.

The range of infrared templates required to understand the 4.5–500 μm SEDs, with a range of a factor of 3.8 in their peak wavelength, makes it hard to determine useful redshifts from submillimetre data alone. However, sources whose SEDs peak at 350 or 500 μm are likely to have $z > 1$.

The requirement of association of our sample with the SWIRE Photometric Redshift Catalogue biases our sample against higher redshift (>1.5) since many higher redshift galaxies would be too weak at 24 μm to be in the SWIRE sample or too faint optically to acquire photometric redshifts. Our sample contains 23 galaxies with $z > 1.5$: the true number in a complete sample would be ∼80. Even so we confirm the result of Clements et al. (2008) that there is a strong tail in the redshift distribution of submillimetre galaxies to lower z.

ACKNOWLEDGMENTS

SPIRE has been developed by a consortium of institutes led by Cardiff University (UK) and including University of Lethbridge (Canada); NAOC (China); CEA, LAM (France); IFSI, University of Padua (Italy); IAC (Spain); Stockholm Observatory (Sweden); Imperial College London, RAL, UCL-MSSL, UKATC, University of Sussex (UK); Caltech, JPL, NHSC, University of Colorado (USA). This development has been supported by national funding agencies: CSA (Canada); NAOC (China); CEA, CNES, CNRS (France); ASI (Italy); MCINN (Spain); SNSB (Sweden); STFC (UK) and NASA (USA).

The data presented in this paper will be released through the *Herschel* data base in Marseille HeDaM.[2]

REFERENCES

Alton P. B. et al., 1998, A&A, 335, 807
Buat V. et al., 2010, MNRAS, in press
Clements D. L. et al., 2008, MNRAS, 387, 247
Dale D. A., Helou G., Contursi A., Silbermann N. A., Kolhatkar S., 2001, ApJ, 549, 215
Dopita M. A. et al., 2005, ApJ, 619, 755
Draine B. T., Li A., 2006, ApJ, 657, 810
Dullemond C. P., van Bemmel I. M., 2005, A&A, 436, 47
Efstathiou A., Rowan-Robinson M., 1995, MNRAS, 273, 649
Efstathiou A., Rowan-Robinson M., 2003, MNRAS, 343, 322
Efstathiou A., Siebenmorgen R., 2009, A&A, 502, 541
Efstathiou A., Rowan-Robinson M., Siebenmorgen R., 2000, MNRAS, 313, 734
Elbaz D. et al., 2010, A&A, in press
Farrah D. et al., 2008, ApJ, 677, 957
Fritz J., Franceschini A., Hatziminaoglou E., 2006, MNRAS, 366, 767
Granato G. L., Danese L., 1994, MNRAS, 268, 235
Griffin M. et al., 2010, A&A, in press
Hernan-Caballero A. et al., 2009, MNRAS, 395, 1695
Hönig S. F., Beckert T., Ohnaka K., Weigelt G., 2006, A&A, 452, 459
Nenkova M., Ivezic Z., Elitzur M., 2002, ApJ, 570, L9
Nenkova M. et al., 2008, ApJ, 685, 147
Oliver S. J. et al., 2010a, MNRAS, submitted
Oliver S. J. et al., 2010b, A&A, submitted
Pier G. L., Krolik J., 1992, ApJ, 401, 99
Pilbratt G. et al., 2010, A&A, in press
Piovan L., Tantalo R., Chiosi C., 2006, MNRAS, 366, 923
Roseboom I. et al., 2010, MNRAS, submitted
Rowan-Robinson M., 1992, MNRAS, 258, 787
Rowan-Robinson M., 1995, MNRAS, 272, 737
Rowan-Robinson M., 2001, ApJ, 549, 745
Rowan-Robinson M., Crawford J., 1989, MNRAS, 238, 523
Rowan-Robinson M., Efstathiou A., 1993, MNRAS, 263, 675
Rowan-Robinson M., Efstathiou A., 2009, MNRAS, 399, 615
Rowan-Robinson M. et al., 2004, MNRAS, 351, 1290
Rowan-Robinson M. et al., 2005, AJ, 129, 1183
Rowan-Robinson M. et al., 2006, in *Spitzer* Conference, Understanding Galaxy Populations, preprint (astro-ph/0603737)
Rowan-Robinson M. et al., 2008, MNRAS, 386, 697
Schartmann M., Meisenheimer K., Camenzind M., Wolf S., Tristram K. R. W., Henning T., 2008, A&A, 482, 67
Siebenmorgen R., Krugel E., 1992, A&A, 259, 614
Siebenmorgen R., Krugel E., 2007, A&A, 461, 445
Silva L., Granato G. L., Bressan A., Danese L., 1998, ApJ, 509, 103
Spoon H. et al., 2007, ApJ, 654, L49
Symeonidis M., Page M. J., Seymour N., Dwelly T., Coppin K., McHardy I., Rieke G. H., Huynh M., 2009, MNRAS, 397, 1728
Takagi T., Arimoto N., Hanami H., 2003, MNRAS, 340, 813

[2] http://hedam.oamp.fr/HerMES

This paper has been typeset from a TEX/LATEX file prepared by the author.